remote sensing

MDPI

Technical Note

A Catalogue of Impact Craters and Surface Age Analysis in the Chang'e-6 Landing Area

Yexin Wang [1], Jing Nan [1,2], Chenxu Zhao [1,2], Bin Xie [1,2], Sheng Gou [3], Zongyu Yue [3,4], Kaichang Di [1,4,*], Hong Zhang [5], Xiangjin Deng [5] and Shujuan Sun [1,6]

1 State Key Laboratory of Remote Sensing Science, Aerospace Information Research Institute, Chinese Academy of Sciences, Beijing 100101, China; wangyx@aircas.ac.cn (Y.W.); nanjing23@mails.ucas.ac.cn (J.N.); zhaochenxu22@mails.ucas.ac.cn (C.Z.); xiebin21@mails.ucas.ac.cn (B.X.); sunshujuan@cdu.edu.cn (S.S.)
2 University of Chinese Academy of Sciences, Beijing 100101, China
3 Key Laboratory of Earth and Planetary Physics, Institute of Geology and Geophysics, Chinese Academy of Sciences, Beijing 100029, China; gousheng@mail.iggcas.ac.cn (S.G.); yuezy@mail.iggcas.ac.cn (Z.Y.)
4 Center for Excellence in Comparative Planetology, Chinese Academy of Sciences, Hefei 230026, China
5 Beijing Institute of Spacecraft System Engineering, China Academy of Space Technology, Beijing 100094, China; dengxiangjin@sina.com (X.D.)
6 School of Architecture and Civil Engineering, Chengdu University, Chengdu 610106, China
* Correspondence: dikc@aircas.ac.cn

Abstract: Chang'e-6 (CE-6) is the first sample-return mission from the lunar farside and will be launched in May of 2024. The landing area is in the south of the Apollo basin, inside the South Pole Aitken basin. Statistics and analyses of impact craters in the landing area are essential to support safe landing and geologic studies. In particular, the crater size–frequency distribution information of the landing area is critical to understanding the provenance of the CE-6 lunar samples to be returned and can be used to verify and refine the lunar chronology model by combining with the radioisotope ages of the relevant samples. In this research, a digital orthophoto map (DOM) mosaic with a resolution of 3 m/pixel of the CE-6 landing area was generated from the 743 Narrow Angle Camera of the Lunar Reconnaissance Orbiter Camera. Based on the DOM, craters were extracted by an automated method and checked manually. A total of 770,731 craters were extracted in the whole area of 246 km × 135 km, 374,684 of which were within the mare area. Systematic analyses of the crater distribution, completeness, spatial density, and depth-to-diameter ratio were conducted. Geologic model age estimation was carried out in the mare area that was divided into three geologic units according to the TiO_2 abundance. The result showed that the east part of the mare had the oldest model age of $\mu 3.27^{+0.036}_{-0.045}$ Ga, and the middle part of the mare had the youngest model age of $\mu 2.49^{+0.072}_{-0.073}$ Ga. The crater catalogue and the surface model age analysis results were used to support topographic and geologic analyses of the pre-selected landing area of the CE-6 mission before the launch and will contribute to further scientific research after the lunar samples are returned to Earth.

Keywords: Chang'e-6; landing area; crater catalogue; surface age; lunar farside

check for updates

Citation: Wang, Y.; Nan, J.; Zhao, C.; Xie, B.; Gou, S.; Yue, Z.; Di, K.; Zhang, H.; Deng, X.; Sun, S. A Catalogue of Impact Craters and Surface Age Analysis in the Chang'e-6 Landing Area. *Remote Sens.* **2024**, *16*, 2014. https://doi.org/10.3390/rs16112014

Academic Editor: Christian Wöhler

Received: 25 April 2024
Revised: 30 May 2024
Accepted: 1 June 2024
Published: 4 June 2024
Corrected: 4 September 2025

Copyright: © 2024 by the authors. Licensee MDPI, Basel, Switzerland. This article is an open access article distributed under the terms and conditions of the Creative Commons Attribution (CC BY) license (https://creativecommons.org/licenses/by/4.0/).

1. Introduction

Lunar samples have been returned to Earth by six Apollo missions (Apollo 11, 12, 14, 15, 16, and 17), three Luna missions (Luna 16, 20, and 24), and the Chang'e-5 mission. The analysis results of these samples are invaluable to our fundamental understanding of lunar origin and evolution [1–4]. Based on the lunar sample radiometric ages, the Moon also provides the foundation of crater size–frequency distribution chronologies for the solar system [5–8]. However, all of the samples were returned from the lunar nearside, and the samples from the farside, especially from the lunar South Pole Aitken (SPA) basin, are crucial to address other fundamental questions such as the nature of the Moon's asymmetry, the composition and structure of the lunar mantle, etc. The Chang'e-6 (CE-6) mission is

scheduled to launch in May of 2024. The pre-selected landing area of CE-6 is in the south of the Apollo basin, a ~490 km diameter crater, within the SPA basin [9,10]. It is the first sample-return mission to the lunar farside and is expected to return the farside basalts.

Impact craters are one of the most prominent surface features of the lunar surface, and they are important in studying the subsurface structure of the Moon [11], tracing the sample source area [12], analyzing the impact flux of the meteorites [8], etc. For comprehensive studies of the impact craters, many global or regional crater catalogues have been established [13–16]. The completeness diameter of the current global crater databases is too large for the CE-6 landing area (e.g., 1 km in [13]) in carrying out scientific analysis on the lunar samples. Zeng et al. mapped 26,785 craters using the 7 m/pixel resolution Chang'e-2 (CE-2) digital orthophoto map (DOM) in the pre-selected CE-6 landing area [10]. However, their work mainly focused on studying the geologic background of the CE-6 landing area, with no particular analysis on the mapped craters such as the completeness diameter that would greatly hinder its further application. Therefore, a detailed study of the impact craters in the CE-6 landing area using higher-resolution images is still necessary.

In this research, we utilized a seamless DOM mosaic based on the Lunar Reconnaissance Orbiter Camera (LROC) Narrow Angle Camera (NAC) images and SLDEM2015 (a lunar digital elevation model generated by co-registration and combining SELENE TC digital elevation model with LRO laser altimetric data) [17], to obtain a crater catalogue in the pre-selected CE-6 landing area. The resolution of the mosaic was 3.0 m/pixel, and the original images were in suitable illumination conditions. As a result, a more reliable and accurate crater catalogue could be obtained. In addition, with the SLDEM2015, the depth of craters was also automatically measured. The obtained crater catalogue and the analysis results can contribute to the studying of the returned lunar samples and other important issues such as the lunar Late Heavy Bombardment. Combined with the radioisotope ages of the samples, the crater size–frequency distribution information can be used to verify and refine the lunar chronology model, which is of fundamental importance for lunar and planetary sciences.

2. Data and Methods

2.1. LROC NAC Images and SLDEM2015

A high-resolution DOM mosaic of the landing area was generated using 743 LROC NAC images as a base map to extract and measure craters in the CE-6 landing area (Figure 1). The LROC NAC images covered most of the lunar surface with a horizontal resolution of 0.5–2 m and were the highest-resolution orbiter images currently available in the pre-selected landing area [18]. A method for large-area DOM generation was proposed and used to produce the high-resolution orthophoto mosaic of the CE-5 landing area [19] and was also used in this research. According to this method, 743 NAC images were selected first, and the Planetary Data System (PDS) experiment data record (EDR) files of them were downloaded from the PDS Geosciences Node Lunar Orbital Data Explorer website. Next, the SPICE kernels were attached, and radiometric corrections were performed for each image using the Integrated System for Imagers and Spectrometers (ISIS) software (v7.2.0). The planar block adjustment was then utilized to improve the relative positional consistencies of the LROC NAC images of the sub-areas to subpixel level and simultaneously align the NAC images to the control source (SLDEM2015). Subsequently, TPS (Thin Plate Spline)-based image registration was used to reduce geometric inconsistencies between the adjacent sub-area DOM mosaics, ensuring that the final DOM was seamlessly mosaicked over the entire area. Finally, a geometrically seamless DOM mosaic was produced, covering 149°–160° west longitude and 39.7°–44.1° south latitude with a resolution of 3 m/pixel. The detailed mapping method can be found in [19].

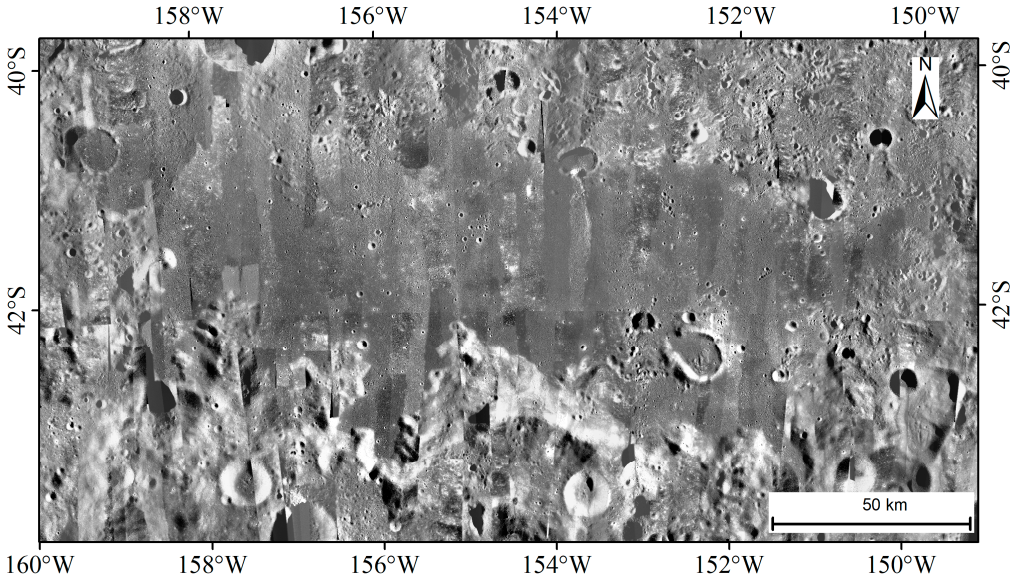


Figure 1. The base map of the CE-6 landing area generated from LROC NAC images with a pixel size of 3 m. The Lambert conformal conic projection was adopted.

SLDEM2015 covered latitudes within ±60° with a horizontal resolution of approximately 60 m in the equator area and a vertical accuracy of 3–4 m. It can be downloaded at the PDS LOLA data node (http://imbrium.mit.edu/EXTRAS/SLDEM2015/, accessed on 10 May 2023). In this research, SLDEM2015 provided the necessary elevation information when generating the DOM mosaic and measuring crater depths in the CE-6 landing area.

2.2. Crater Extraction and Mapping in CE-6 Landing Area

In this research, the impact craters within the CE-6 landing area were extracted using a deep-learning-based automated method followed by manual inspection. Our method was based on the YOLOv8 model (https://github.com/ultralytics/ultralytics, accessed on 15 June 2023), which combines object classification and localization in the same network, directly regressing the position and class information of the object in an end-to-end manner [20]. Our improved YOLOv8-LCNET (YOLOv8-lunar crater net) integrated more pyramid levels to extract craters with a wide range of diameter spans. Comparing with the former versions of YOLO, our improved YOLOv8-LCNET demonstrated higher recall rate in the lunar crater extraction task. As the focus of this paper was the analysis of the extracted craters of the landing area, the technical details of YOLOv8-LCNET will not be elaborated. A comparison of the performance of our improved method with the original method can be found in Appendix A. The training of the network and validation of the results are briefly described below.

Within the CE-6 landing area, a local mosaic DOM map with a resolution better than one meter was produced, based on which the crater sample dataset was established using the same approach of automatic extraction followed by manual inspection. The local DOM mosaic was cropped to sub images of 512 × 512 pixels to form the dataset, which contained 66,030 impact crater samples with a range in diameter from 3.7 m to 609 m. In addition, in order to improve the generalization of YOLOv8-LCNET, random data augmentation techniques such as flipping, rotation, adding noise, and image enhancement were applied to generate a dataset comprising 209,627 sample images. The dataset was split into training and validation datasets in the ratio of 8:2 for model training and performance evaluation.

To assess the rim accuracy of the impact craters automatically extracted by YOLOv8-LCNET, the diameters of the extracted craters and the manually confirmed true values were compared (Figure 2). As shown in Figure 2, an optimal straight line fitted from the scattering points plotted by the diameters automatically measured from the extracted craters and the true diameters had a slope of 1.034 and an intercept of 0.411 in meters. Additionally,

the mean relative error (MRE) of the diameters was calculated to be 0.1042 (i.e., 10.42% diameter difference). These findings indicated that the automatically extracted impact crater diameters were consistent with the true diameters. This consistency verified the agreement between automatic extraction and manual extraction methods, thus demonstrating that the YOLOv8-LCNET algorithm could replace most of the manual efforts in impact crater extraction. It is worth mentioning that for manual crater mapping, different workers would generate different results, with up to 10% diameter differences [21]. In this research, the approach of automatic crater extraction and manual checking proved to be practical and time-saving.

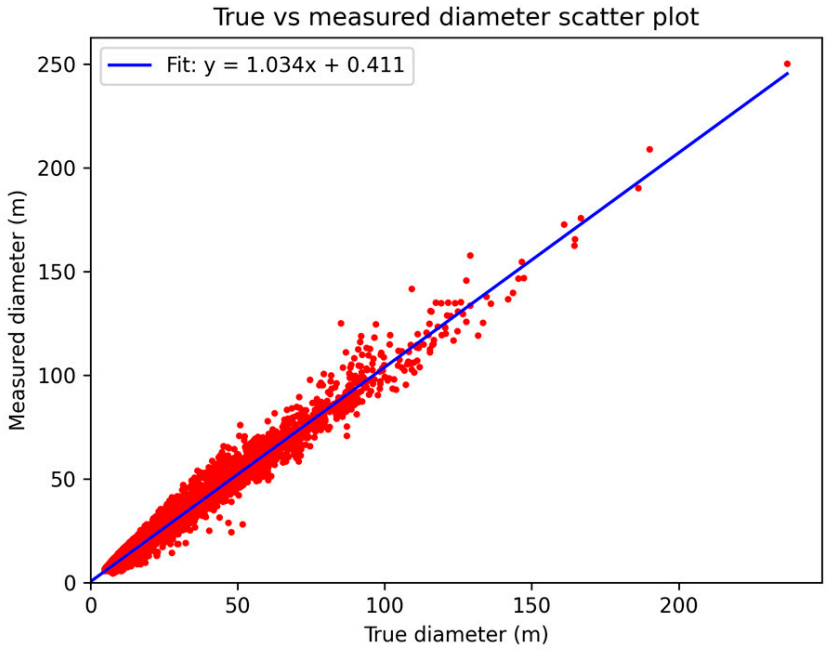


Figure 2. Comparison between the diameters automatically measured from extracted craters and diameters of the manually confirmed craters.

Note that the rims of the craters were first extracted and then transformed into local projection coordinate systems, ensuring that the crater measurements were not affected by map projection. After the automatic extraction by YOLOv8-LCNET, manual inspection work was conducted to erase some false detections and add missing detections from the DOM mosaic with an ArcGIS extension named "CraterTools" [22]. All crater extraction results were manually examined using this tool, especially for impact craters larger than 200 m for dating purposes. Due to significant differences in the solar azimuth and elevation angles of some images forming the DOM mosaic, the manual examination was mainly needed in regions with extreme solar elevation angles or where large craters were in two images with contrary azimuth angles.

To calculate the crater rim-to-floor depth, an automatic tool developed by [23] was utilized. For each crater, profiles crossing the crater center were generated every 22.5° to form a total number of 8. Then a local maximum of the topographic curvature in each profile was found within 10% of the diameter on both sides of the crater circle. The resultant 16 rim points were used to represent the crater rims in order to obtain an averaged rim-to-floor depth of the crater. Note that in some cases such as craters intersecting with other craters, the interfered rim points were eliminated automatically. If fewer than 6 rim points were left, manually added rim points were needed. More details about the automatic crater rim-to-floor tool can be found in [23]. As the resolution of SLDEM2015 constrained small crater rim-to-floor depth calculation, craters larger than 8 pixels were selected for this automatic depth measurement [15,24].

In order to carry out surface dating, secondary craters needed to be removed from the dataset. Based on the appearance of clusters and chains around a primary crater with ejecta patterns, secondary craters were recognized and removed manually.

2.3. Surface Dating with Craters

Absolute ages can provide vital information in establishing the geologic history of the Moon, and currently, the widely used surface dating method is based on the crater size–frequency distribution (CSFD). The method was elaborated by [5] and was the subject of many papers (e.g., [25,26]). The rationale of the method was to fit the observed CSFD of a counting area to a known crater production function (PF) (e.g., [27,28]), which was further used to derive the absolute age along with a chronology function (CF) calibrated to radiometric dating of the returned lunar samples [5]. The detailed steps of the method can be summarized as follows: (1) obtaining the CSFD of a counting area belonging to the same geologic unit, (2) comparing it with a known crater production function (PF) [27,28], and (3) deriving the absolute age according to a CF that has been calibrated to radiometric dating of the returned lunar samples [5]. In practical work, these calculations are often completed with the aid of CraterStats software (v2.0) [28].

The titanium dioxide (TiO_2) content of lunar mare basalt represents an important indicator in magma evolution and is widely used to classify lunar basalt types [29]. According to the TiO_2 abundance derived from LROC WAC imageries by [30] and the basalt classification schema [29], three areas (i.e., A1, A2, and A3) within the basalt unit [31] for the CE-6 potential landing and sampling region inside the Apollo basin were outlined for crater dating in this study (shown in Figure 3), with the TiO_2 abundances of them being 4.6 ± 1.0%, 6.2 ± 1.3%, and 3.8 ± 0.8%, respectively.

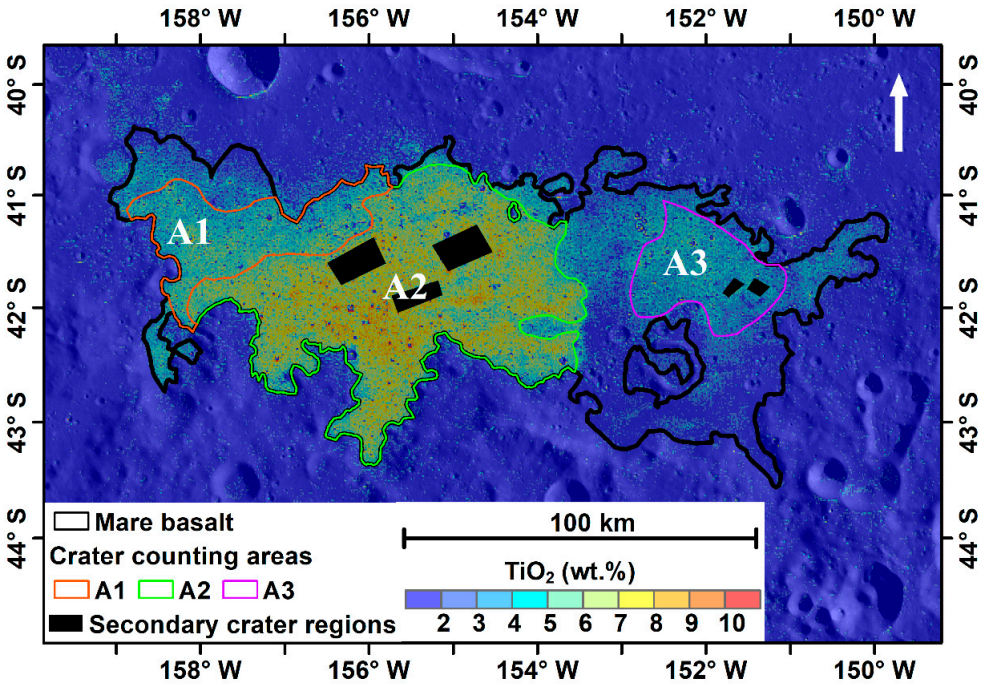


Figure 3. Crater dating areas (i.e., A1, A2, and A3) of the basalt inside the Apollo basin. The basemap is the TiO_2 abundance [30] overlying the LROC Wide Angle Camera global mosaic [32]. The black polygon is the mare extent defined by [31]. The red, green, and magenta polygons are the crater counting areas of A1, A2, and A3. The black patches inside A2 and A3 are regions excluded for counting due to contamination of secondary craters.

3. Results

3.1. Catalogue of Craters in CE-6 Landing Area

In this 246 km × 135 km landing area, a total number of 770,731 craters were extracted using the approach introduced in Section 2.2. According to the properties of the area surface, the whole area could be divided into mare and highland. The number of impact craters in the mare region is 374,684. The completeness diameter size for these craters was calculated within the mare area and is shown in Figure 4.

The completeness value of a crater dataset means that all the craters with diameters larger than this value are included [33]. Previous studies developed three different approaches of estimating the crater diameter completeness [33–35]. Salamunićcar et al. considered the completeness diameter as the inflection point of the slope in the cumulative CSFD curve of impact craters [34]. Robbins and Hynek adopted the value of the completeness diameter from the diameter of the bin one size larger than the bin with the highest number of impact craters in the incremental CSFD [35]. According to Robbins [33], the value was estimated by the Nth diameter bin larger than where the derivative of the slope was zero in an incremental CSFD.

Figure 4a,b illustrate the incremental and cumulative CSFD, respectively, of the craters in the mare area. In Figure 4a, the diameter of the crater cluster with the maximum number is approximately 25 m, yielding a completeness diameter of approximately 30 m according to the definition of Robbins and Hynek [35]. In Figure 4b, the inflection point of the slope is approximately 20 m. In Figure 4c, the value given by Robbins' method is approximately 170 m [33]. Robbins' value was larger compared with the other two, which may have been due to crater saturation equilibrium in the mare region. As the resolution of the mosaic map was 3 m/pixel, the completeness analysis result illustrated by Figure 4a,b indicates that the craters with diameters no less than 10 pixels were extracted. This dense crater catalogue can provide rich information for multiple applications such as landing safety evaluation, crater formation mechanisms, and impact gardening effects, etc. [36].

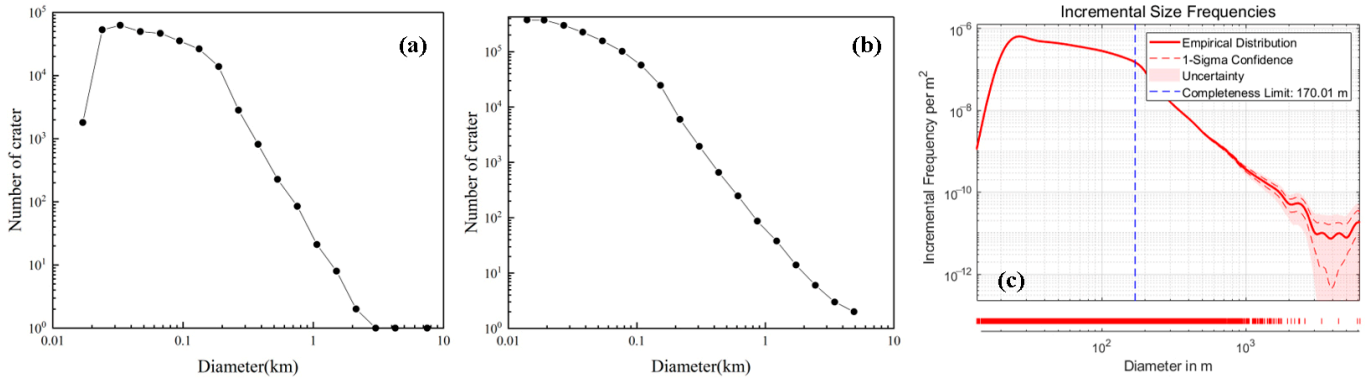


Figure 4. The (**a**) incremental and (**b**) cumulative size–frequency distributions of craters in the crater catalogue with the diameter internal of $\sqrt{2}$D in a log-log plot. Note that the diameter axis is the crater median in each bin. (**c**) The incremental size–frequency distribution established by robust kernel density estimation [33].

In this crater catalogue of the whole area, 38,471 possible secondary crater clusters were identified and eliminated by the easily applicable criteria of irregular shape, clustered distribution, and auxiliary information of shallow depth. In the original crater catalogue, there were 511,484 craters with diameters larger than 30 m, 15,575 craters with diameters larger than 200 m, and 456 craters with diameters larger than 1 km. The mapping results showing craters with diameters ≥200 m are illustrated in Figure 5. After secondary crater elimination, there were 484,410 craters with diameters larger than 30 m, 14,142 craters with diameters larger than 200 m, and 415 craters with diameters larger than 1 km.

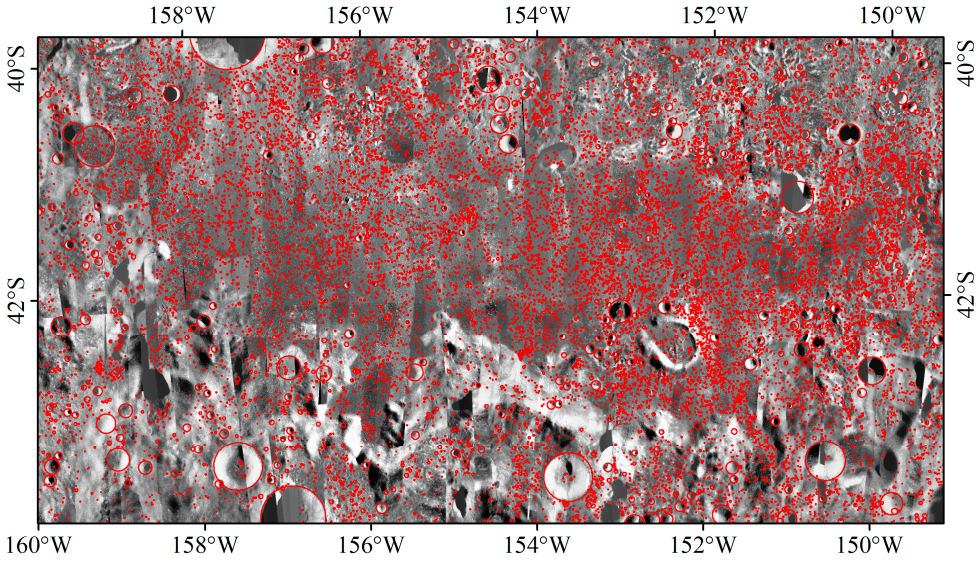


Figure 5. The mapped craters annotated in red with diameters larger than 200 m in the CE-6 landing area overlaying on the LROC NAC DOM mosaic.

Spatial density analysis was conducted on the catalogue after exclusion of secondary craters and on two subsets of greater than 30 m and greater than 1 km, respectively. As shown in Figure 6a,b, the spatial density of impact craters ranging from 30 m to 1 km was greater in the mare region at the center of the landing area than in the highlands. For craters with diameters greater than 1 km, they were more commonly found in the highlands than in the mare. This was because some of the small impact craters in the highlands were expunged due to topographic relief, while the large impact craters were preserved.

The estimation of crater depth was based on SLDEM2015, which is described in Section 2.2. Considering the grid size of SLDEM2015, only craters with diameters larger than 480 m were considered for depth estimation. Craters with depths larger than 12 m were utilized for subsequent analysis, considering the vertical accuracy of SLDEM2015 to be 3–4 m. A total of 1547 craters were ultimately measured for depth, with depths ranging from 12.1 to 2583.8 m. The majority of craters (94.2%) had depths less than 200 m. Six craters were deeper than 1 km, and nearly all of these craters were located in the geological units of the highlands. Figure 7 shows the crater depth distribution with a depth interval of 50 m.

In this work, the depth-to-diameter ratio was used to assess the morphology of craters. The depth-to-diameter ratios of a total number of 1,547 craters were calculated in the mare and highlands (as shown in Figure 3). The statistical results of the depth-to-diameter ratios are shown in Figure 8. As shown in Figure 8a, the depth-to-diameter ratio in the mare region was higher than that of the highland, which was because of the younger age of the mare, as well as the crater size difference illustrated in Figure 6. In the highlands, there were 1132 craters with diameters ranging from 480 to 19,882 m and depths from 12.1 to 2583.8 m, resulting in an average depth-to-diameter ratio of 0.058. In the mare area, there were 415 craters with diameters ranging from 481 to 6179 m and depths from 12.3 to 313.2 m, resulting in an average depth-to-diameter ratio of 0.071. Although the average depth-to-diameter ratios differed, the ranges of them were almost the same in both regions as shown in Figure 8b. Qualitative morphological analyses were also carried out, some examples can be found in Appendix B.

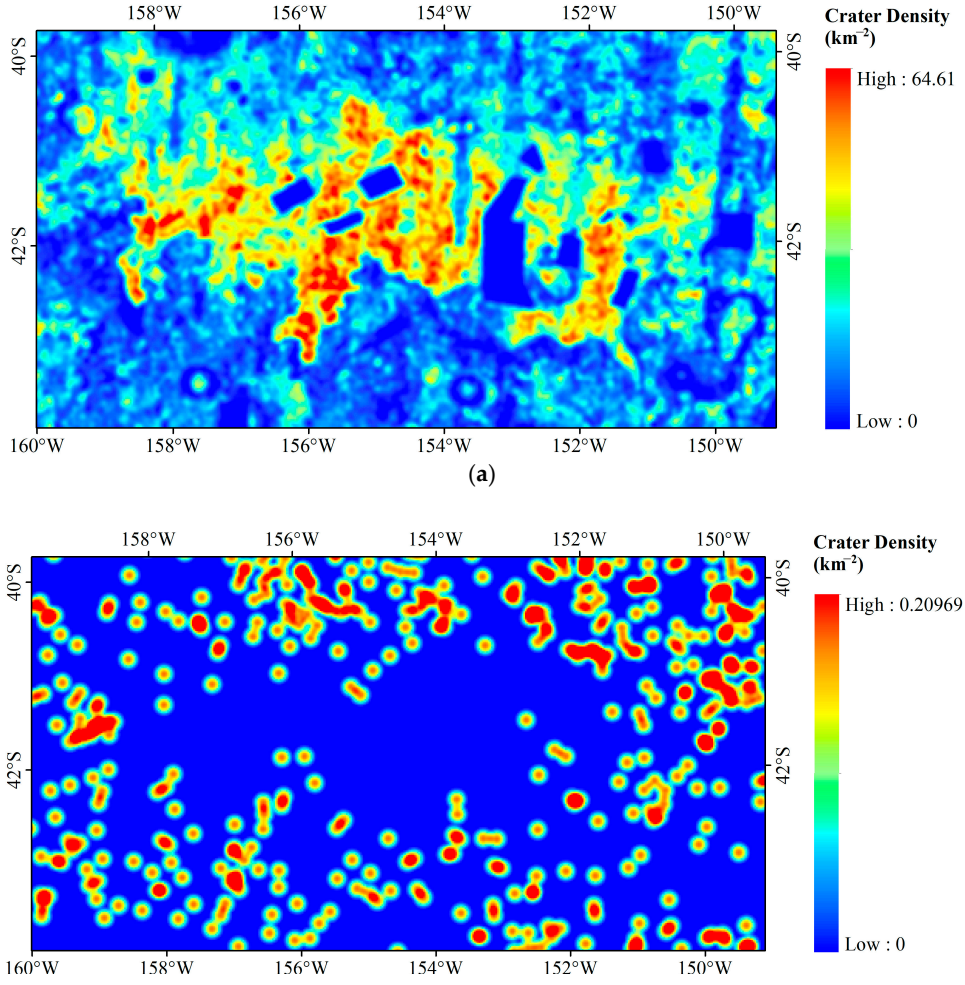


Figure 6. Spatial densities of craters in the CE-6 landing area: (**a**) spatial density of the crater diameters within 30 m to 1 km excluding possible secondary craters and (**b**) spatial density of craters with $D \geq 1$ km excluding possible secondary craters. The Lambert conformal conic projection is adopted. Note that the colors represent different density values in different plots.

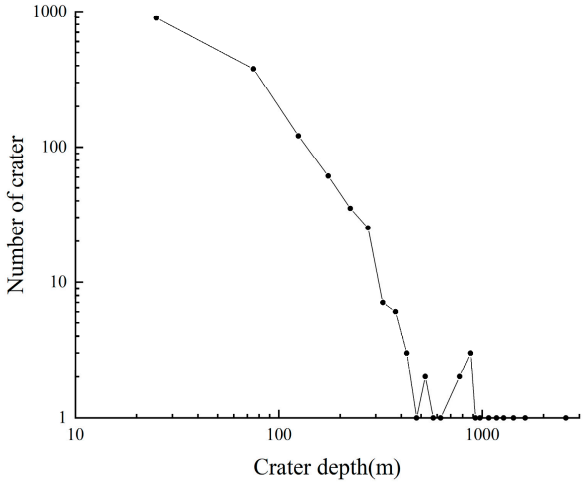


Figure 7. Crater depth (D > 480 m) distribution of CE-6 landing area in a log-log plot. There are 1547 craters catalogued with a depth interval of 50 m.

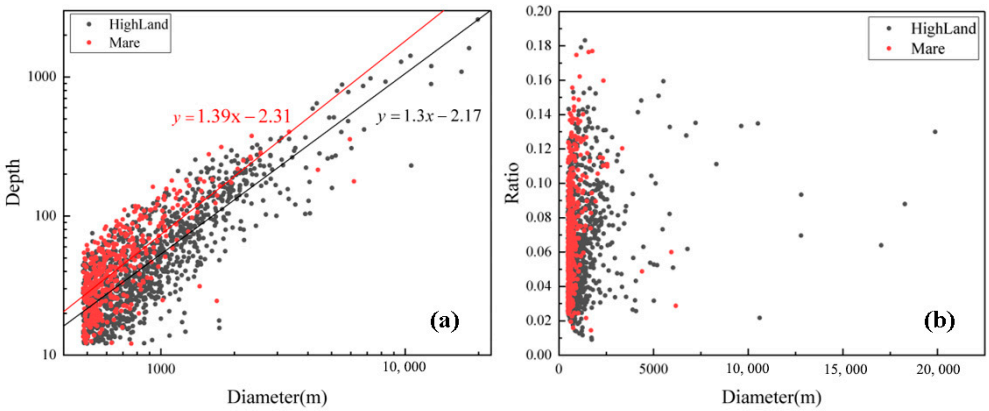


Figure 8. The relationships between the crater diameter and (**a**) the crater depth (in a log-log plot) and (**b**) the d-D ratio. The results for mare craters are shown in red, while the results for highland are shown in black.

3.2. Surface Model Ages of CE-6 Landing Area

By inputting impact crater extraction results into the CraterStats software, the absolute model ages (AMAs) of the A1, A2, and A3 basalt units were $\mu 2.62^{+0.093}_{-0.095}$ Ga, $\mu 2.49^{+0.072}_{-0.073}$ Ga, and $\mu 3.27^{+0.036}_{-0.045}$ Ga, respectively (Figure 9a–c). The AMAs of A1 and A2 were within each other's uncertainty range, suggesting there might be either two basalt flooding events or only one flooding event, but the surface of A1 was masked/contaminated by materials with low TiO_2 content (e.g., ejecta) that resulted in a decrease in TiO_2 abundance. If the latter was the case, dating on the A1 + A2 unit would indicate the flooding happened around $\mu 2.58^{+0.063}_{-0.064}$ Ga (Figure 9d).

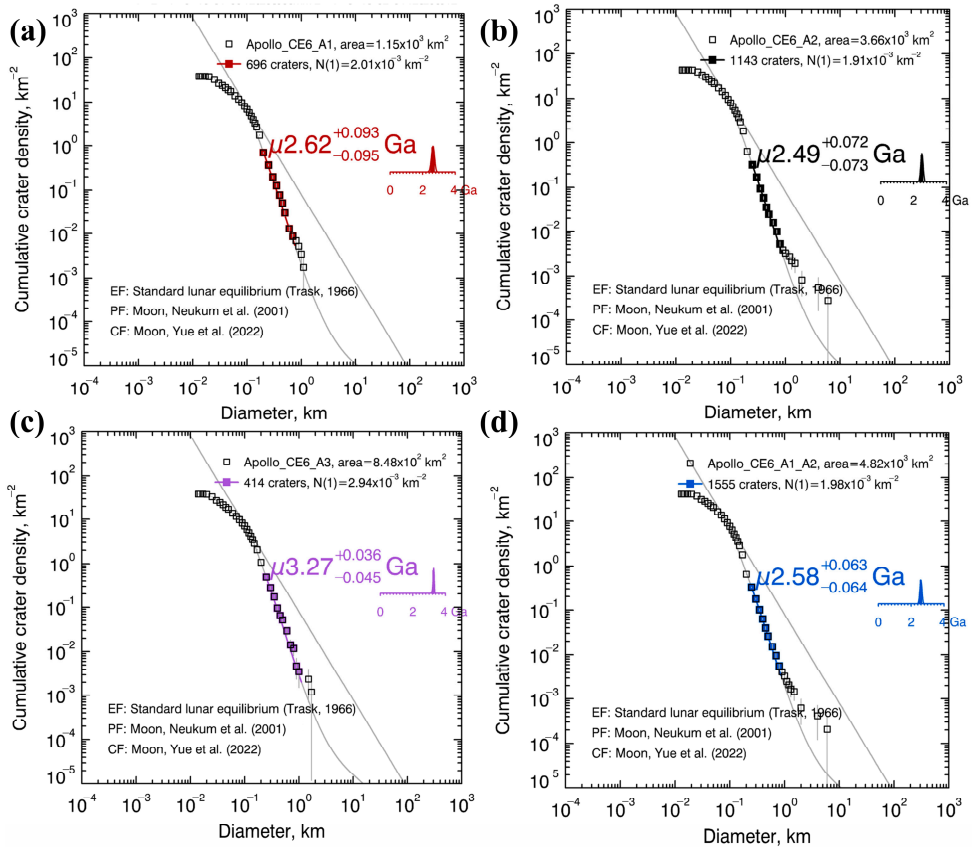


Figure 9. AMAs of the crater dating areas: (**a**) A1; (b) A2; (**c**) A3; (**d**) A1 + A2. The standard lunar crater equilibrium line is from [37], the PF is from [38], and the CF is from [8].

4. Discussion

4.1. Comparison with the Craters in CE-5 Landing Area

The completeness analysis of the mare region using three different methods provided varying values, which is introduced in Section 3.2. The value provided by Robbins' method was much larger than the other two methods. This was because the method adopted the production function, which took the crater saturation equilibrium into account [33]. From Figure 9a–c, the three basalt units, covering most of the mare region, also showed that the craters were essentially saturated at diameters greater than 100 m.

As described in Section 3.2, the depth–diameter ratios of the mare and highland areas in the CE-6 landing area were 0.071 and 0.058, respectively, which coincided with the conclusion from [39] that small craters (less than ~4 km in diameter) on the lunar maria were found to be deeper than those on the highlands. The highland area in the CE-6 landing area contained 415 craters larger than 1 km, which was almost twice the amount of the CE-5 landing area; therefore, the overall depth–diameter ratio distributions showed smaller values than that of the CE-5 landing area.

4.2. Dating Results Compared with Previous Study

Ref. [10] also carried out crater dating on the basalt units of the CE-6 landing area, with approximately similar dating areas of A2 and A3. They used the classic chronology system, i.e., [5]. If the chronology system from [5] was used for dating in this study, the AMAs of the A1, A2, A3, and A1 + A2 basalt units were $\mu 2.51^{+0.092}_{-0.094}$ Ga, $\mu 2.38^{+0.07}_{-0.07}$ Ga, $\mu 3.25^{+0.043}_{-0.056}$ Ga, and $\mu 2.46^{+0.062}_{-0.062}$ Ga, respectively (Figure 10a–c). Compared with their dating results (i.e., $2.40^{+0.11}_{-0.11}$ Ga for the F_A unit and $3.43^{+0.044}_{-0.061}$ for the L_A unit), the AMA of the A2 unit was about the same in both studies, while the AMA of the A3 unit estimated in this study was younger than that of [10]. The difference might be because the dating regions and data sources for crater counting were not completely consistent. Overall, as we mapped craters based on higher-resolution DOM and used more craters in dating the surface units after eliminating secondary craters, our surface dating results should be more reliable.

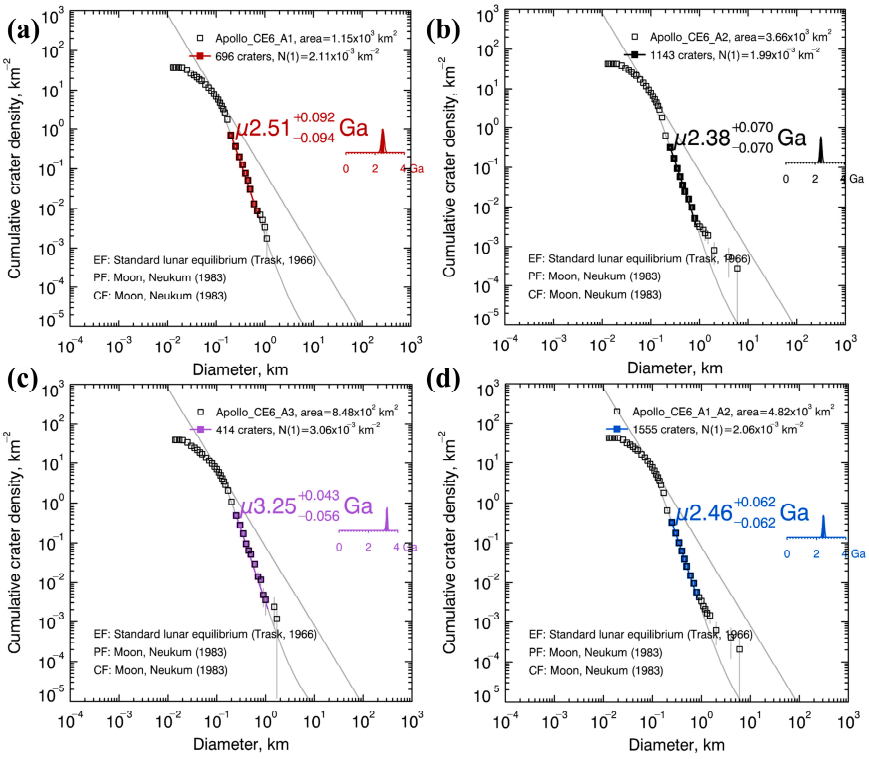


Figure 10. AMAs of the crater dating areas: (**a**) A1; (**b**) A2; (**c**) A3; (**d**) A1 + A2. The standard lunar crater equilibrium line is from [37], the PF is from [5], and the CF is from [5].

5. Conclusions

We established a catalogue of 770,731 craters with the completeness diameter of 30 m in the CE-6 landing area based on an LROC NAC DOM mosaic with resolution of 3 m/pixel. The craters were extracted by our improved YOLOv8-LCNET deep-learning algorithm and examined manually. The morphology and distribution of all the craters and the depth analysis of craters larger than 480 m were included in this catalogue. The crater size-frequencies of different surface units delineated by TiO_2 abundance were analyzed to obtain the absolute model ages. The results showed that the oldest unit lay in the right of the mare and had a model age of $\mu 3.27^{+0.036}_{-0.045}$ Ga, and the youngest unit was the middle part of the mare, which had a model age of $\mu 2.49^{+0.072}_{-0.073}$ Ga. The established crater catalogue was used to support topographic and geologic analyses of the pre-selected landing area of the CE-6 mission for landing safety evaluation and scientific research before the launch. The catalogue and the derived surface ages have multiple potential applications after the lunar samples are returned. This catalogue and the CSFD analysis results will be helpful for the interpretation of the samples and understanding their provenances, the lunar chronology model refinement when combined with the radioisotope ages of the relevant samples, and better understanding of the geologic properties of the landing site, the Apollo basin, and the SPA basin.

Author Contributions: Conceptualization, Y.W., K.D. and Z.Y.; methodology, J.N., B.X., Z.Y., S.G. and S.S.; formal analysis, C.Z. and S.G.; investigation, C.Z., S.G., H.Z. and X.D.; resources, B.X.; data curation, J.N., C.Z. and B.X.; writing—original draft preparation, all the authors; writing—review and editing, Y.W., S.G., Z.Y., K.D. and S.S.; visualization, C.Z. and S.G.; supervision, K.D.; project administration, Y.W.; funding acquisition, K.D. All authors have read and agreed to the published version of the manuscript.

Funding: This research was funded by the National Key Research and Development Program of China (Grant No. 2022YFF0503100), the Strategic Priority Research Program of the Chinese Academy of Sciences (grant No. XDB41000000), and the Open Fund of State Key Laboratory of Remote Sensing Science (Grant No. OFSLRSS202206).

Data Availability Statement: The craters used for surface model ages dating presented in the study are openly available in Zenodo at https://doi.org/10.5281/zenodo.11385444 (accessed on 31 May 2024). The remaining data supporting the conclusions of this article will be made available by the authors on request.

Acknowledgments: The authors gratefully acknowledge all those who worked on the Planetary Data System archive (https://ode.rsl.wustl.edu/moon/index.aspx, accessed on 10 May 2023) to make the LROC NAC imagery and SLDEM2015 publicly available.

Conflicts of Interest: The authors declare that they have no known competing financial interests or personal relationships that could have appeared to influence the work reported in this paper.

Appendix A

To evaluate the performance of the proposed YOLOv8-LCNET network, we compared the crater extraction results using this improved and the original YOLOv8 networks. The training dataset and training parameters used for two networks were the same. The crater extraction results tested on the validation dataset are shown in Table A1. Table A1 indicates that compared with the original YOLOv8 algorithm, the proposed YOLOv8-LCNET network had significant improvements on Precision, Recall, mAP50, and mAP50-95 of 0.228, 0.312, 0.439, and 0.350, respectively, which meant YOLOv8-LCNET reduced manual work better than using YOLOv8.

Table A1. Performance comparisons of YOLOv8 and YOLOv8-LCNET.

Model	Precision	Recall	mAP50	mAP50-95
YOLOv8	0.630	0.516	0.547	0.325
YOLOv8-LCNET	0.858	0.828	0.906	0.675

Appendix B

In this work, simple qualitative morphological analyses of the extracted craters have also been conducted. Figure A1 provides some examples showing different depth-to-diameter ratios of craters at various degradation stages. From Figure A1a–c, it is obvious to distinguish the different stages of the crater degradation according to the morphological characteristics. And the quantitative calculation of the depth-to-diameter ratios coincides with the intuition of visual interpretation. The crater catalogue we established provides a base dataset to carry out more comprehensive work on integrating qualitative and quantitative analyses for better understanding of crater degradation mechanism.

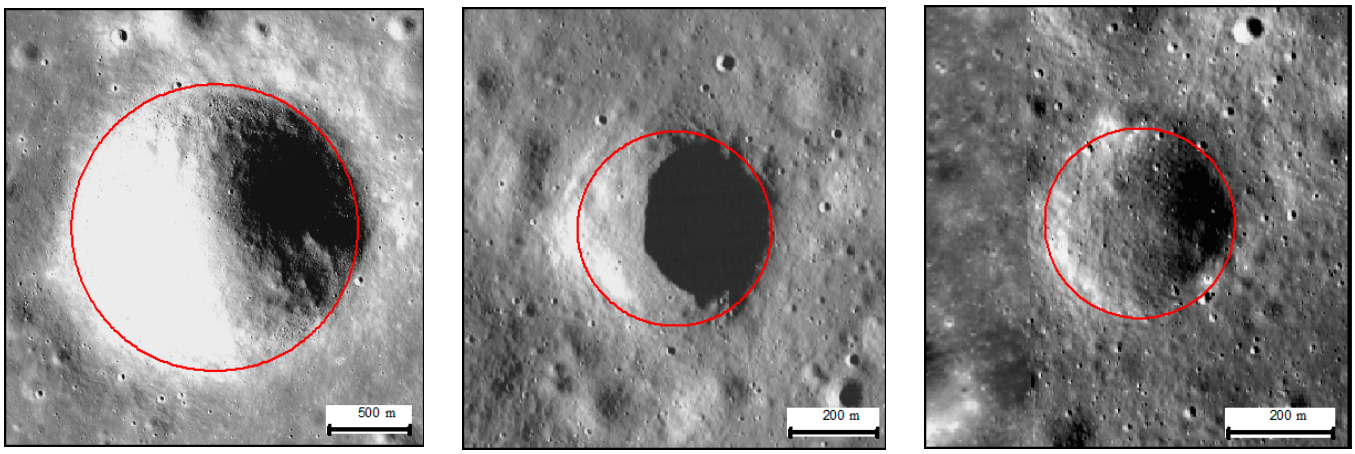


Figure A1. Different depth-to-diameter ratios of craters at various degradation stages: (**a**) a fresh crater (location: 156.07°W, 41.59°S) with diameter of 1769.7 m and depth-to-diameter ratio of 0.177, (**b**) a degraded crater (location: 152.80°W, 40.58°S) with diameter of 453.2 m and depth-to-diameter ratio of 0.07, and (**c**) a heavily degraded crater (location: 158.02°W, 41.59°S) with diameter of 364 m and depth-to-diameter ratio of 0.023.

References

1. Smith, J.V.; Anderson, A.T.; Newton, R.C.; Olsen, E.J.; Crewe, A.V.; Isaacson, M.S. Petrologic history of the moon inferred from petrography, mineralogy and petrogenesis of Apollo 11 rocks. In Proceedings of the Apollo 11 Lunar Science Conference, Houston, TX, USA, 5–8 January 1970; p. 897.
2. Wood, J.A.; Dickey, J.J.S.; Marvin, U.B.; Powell, B.N. Lunar anorthosites and a geophysical model of the moon. In Proceedings of the Apollo 11 Lunar Science Conference, Houston, TX, USA, 5–8 January 1970; p. 965.
3. Stevenson, D.J. Origin of the Moon-The Collision Hypothesis. *Annu. Rev. Earth Planet Sci.* **1987**, *15*, 271–315. [CrossRef]
4. Hu, S.; He, H.; Ji, J.; Lin, Y.; Hui, H.; Anand, M.; Tartèse, R.; Yan, Y.; Hao, J.; Li, R.; et al. A dry lunar mantle reservoir for young mare basalts of Chang'e-5. *Nature* **2021**, *600*, 49–53. [CrossRef] [PubMed]
5. Neukum, G. *Meteoriten Bombardement und Datierung Planetarer Oberflächen (Meteorite Bombardment and Dating of Planetary Surfaces)*; Ludwig-Maximilians University: Munich, Germany, 1983.
6. Ivanov, B.A. Mars/Moon Cratering Rate Ratio Estimates. *Space Sci. Rev.* **2001**, *96*, 87–104. [CrossRef]
7. Yue, Z.; Di, K.; Michael, G.; Gou, S.; Lin, Y.; Liu, J. Martian surface dating model refinement based on Chang'E-5 updated lunar chronology function. *Earth Planet Sci. Lett.* **2022**, *595*, 117765. [CrossRef]
8. Yue, Z.; Di, K.; Wan, W.; Liu, Z.; Gou, S.; Liu, B.; Peng, M.; Wang, Y.; Jia, M.; Liu, J.; et al. Updated lunar cratering chronology model with the radiometric age of Chang'e-5 samples. *Nat. Astron.* **2022**, *6*, 541–545. [CrossRef]
9. Li, C.; Wang, C.; Wei, Y.; Lin, Y. China's present and future lunar exploration program. *Science* **2019**, *365*, 238–239. [CrossRef] [PubMed]
10. Zeng, X.; Liu, D.; Chen, Y.; Zhou, Q.; Ren, X.; Zhang, Z.; Yan, W.; Chen, W.; Wang, Q.; Deng, X.; et al. Landing site of the Chang'e-6 lunar farside sample return mission from the Apollo basin. *Nat. Astron.* **2023**, *7*, 1188–1197. [CrossRef]
11. Yue, Z.; Di, K.; Liu, Z.; Michael, G.; Jia, M.; Xin, X.; Liu, B.; Peng, M.; Liu, J. Lunar regolith thickness deduced from concentric craters in the CE-5 landing area. *Icarus* **2019**, *329*, 46–54. [CrossRef]

12. Jia, B.; Fa, W.; Zhang, M.; Di, K.; Xie, M.; Tai, Y.; Li, Y. On the provenance of the Chang'E-5 lunar samples. *Earth Planet Sci. Lett.* **2022**, *596*, 117791. [CrossRef]
13. Robbins, S.J. A New Global Database of Lunar Impact Craters >1–2 km: 1. Crater Locations and Sizes, Comparisons With Published Databases, and Global Analysis. *J. Geophys. Res. Planets* **2019**, *124*, 871–892. [CrossRef]
14. Wang, Y.; Wu, B.; Xue, H.; Li, X.; Ma, J. An Improved Global Catalog of Lunar Impact Craters (≥1 km) With 3D Morphometric Information and Updates on Global Crater Analysis. *J. Geophys. Res. Planets* **2021**, *126*, e2020JE006728. [CrossRef]
15. Jia, M.; Yue, Z.; Di, K.; Liu, B.; Liu, J.; Michael, G. A catalogue of impact craters larger than 200 m and surface age analysis in the Chang'e-5 landing area. *Earth Planet Sci. Lett.* **2020**, *541*, 116272. [CrossRef]
16. Bo, Z.; Di, K.; Liu, Z.; Yue, Z.; Liu, J.; Shi, K. A catalogue of meter-scale impact craters in the Chang'e-5 landing area measured from centimeter-resolution descent imagery. *Icarus* **2022**, *378*, 114943. [CrossRef]
17. Barker, M.K.; Mazarico, E.; Neumann, G.A.; Zuber, M.T.; Haruyama, J.; Smith, D.E. A new lunar digital elevation model from the Lunar Orbiter Laser Altimeter and SELENE Terrain Camera. *Icarus* **2016**, *273*, 346–355. [CrossRef]
18. Robinson, M.S.; Brylow, S.M.; Tschimmel, M.; Humm, D.; Lawrence, S.J.; Thomas, P.C.; Denevi, B.W.; Bowman-Cisneros, E.; Zerr, J.; Ravine, M.A.; et al. Lunar Reconnaissance Orbiter Camera (LROC) Instrument Overview. *Space Sci. Rev.* **2010**, *150*, 81–124. [CrossRef]
19. Di, K.; Jia, M.; Xin, X.; Wang, J.; Liu, B.; Li, J.; Xie, J.; Liu, Z.; Peng, M.; Yue, Z.; et al. High-Resolution Large-Area Digital Orthophoto Map Generation Using LROC NAC Images. *Photogramm. Eng. Remote Sensing* **2019**, *85*, 481–491. [CrossRef]
20. Juan, T.; Diana-Margarita, C.; Julio-Alejandro, R. A Comprehensive Review of YOLO Architectures in Computer Vision: From YOLOv1 to YOLOv8 and YOLO-NAS. *Mach. Learn. Knowl. Extr.* **2023**, *5*, 1680–1716. [CrossRef]
21. Robbins, S.J.; Antonenko, I.; Kirchoff, M.R.; Chapman, C.R.; Fassett, C.I.; Herrick, R.R.; Singer, K.; Zanetti, M.; Lehan, C.; Huang, D.; et al. The variability of crater identification among expert and community crater analysts. *Icarus* **2014**, *234*, 109–131. [CrossRef]
22. Kneissl, T.; van Gasselt, S.; Neukum, G. Map-projection-independent crater size-frequency determination in GIS environments—New software tool for ArcGIS. *Planet Space Sci.* **2011**, *59*, 1243–1254. [CrossRef]
23. Liu, Z.; Yue, Z.; Michael, G.; Gou, S.; Di, K.; Sun, S.; Liu, J. A global database and statistical analyses of (4) Vesta craters. *Icarus* **2018**, *311*, 242–257. [CrossRef]
24. Gou, S.; Yue, Z.; Di, K.; Liu, Z. A global catalogue of Ceres impact craters ≥ 1 km and preliminary analysis. *Icarus* **2018**, *302*, 296–307. [CrossRef]
25. Stöffler, D.; Ryder, G. Stratigraphy and Isotope Ages of Lunar Geologic Units: Chronological Standard for the Inner Solar System. *Space Sci. Rev.* **2001**, *96*, 9–54. [CrossRef]
26. Stöffler, D.; Ryder, G.; Ivanov, B.A.; Artemieva, N.A.; Cintala, M.J.; Grieve, R.A.F. Cratering History and Lunar Chronology. *Rev. Mineral Geochem.* **2006**, *60*, 519–596. [CrossRef]
27. Hiesinger, H.; Jaumann, R.; Neukum, G.; Head III, J.W. Ages of mare basalts on the lunar nearside. *J. Geophys. Res. Planets* **2000**, *105*, 29239–29275. [CrossRef]
28. Michael, G.; Neukum, G. Planetary surface dating from crater size–frequency distribution measurements: Partial resurfacing events and statistical age uncertainty. *Earth Planet Sci. Lett.* **2010**, *294*, 223–229. [CrossRef]
29. Giguere, T.A.; Taylor, G.J.; Hawke, B.R.; Lucey, P.G. The titanium contents of lunar mare basalts. *Meteorit. Planet. Sci.* **2000**, *35*, 193–200. [CrossRef]
30. Sato, H.; Robinson, M.S.; Lawrence, S.J.; Denevi, B.W.; Hapke, B.; Jolliff, B.L.; Hiesinger, H. Lunar mare TiO_2 abundances estimated from UV/Vis reflectance. *Icarus* **2017**, *296*, 216–238. [CrossRef]
31. Nelson, D.; Koeber, S.; Daud, K.; Robinson, M.; Watters, T.; Banks, M.; Williams, N. Mapping Lunar Maria Extents and Lobate Scarps Using LROC Image Products. In Proceedings of the 45th Lunar and Planetary Science Conference, The Woodlands, TX, USA, 17–21 March 2014; p. 2861.
32. Wagner, R.V.; Speyerer, E.J.; Robinson, M.S.; The LROC Team. New Mosaicked Data Products from the LROC Team. In Proceedings of the 46th Lunar and Planetary Science Conference, The Woodlands, TX, USA, 16–20 March 2015; p. 1473.
33. Robbins, S.J.; Riggs, J.D.; Weaver, B.P.; Bierhaus, E.B.; Chapman, C.R.; Kirchoff, M.R.; Singer, K.N.; Gaddis, L.R. Revised recommended methods for analyzing crater size-frequency distributions. *Meteorit. Planet. Sci.* **2018**, *53*, 891–931. [CrossRef]
34. Salamunićcar, G.; Lončarić, S.; Mazarico, E. LU60645GT and MA132843GT catalogues of Lunar and Martian impact craters developed using a Crater Shape-based interpolation crater detection algorithm for topography data. *Planet Space Sci.* **2012**, *60*, 236–247. [CrossRef]
35. Robbins, S.J.; Hynek, B.M. A new global database of Mars impact craters ≥1 km: 2. Global crater properties and regional variations of the simple-to-complex transition diameter. *J. Geophys. Res. Planets* **2012**, *117*, E06001. [CrossRef]
36. Shi, K.; Yue, Z.; Di, K.; Liu, J.; Dong, Z. The gardening process of lunar regolith by small impact craters: A case study in Chang'E-4 landing area. *Icarus* **2022**, *377*, 114908. [CrossRef]
37. Trask, N.J. Size and spatial distribution of craters estimated from the ranger photographs. In *Ranger VIII and IX, Part II—Experimenters' Analyses and Interpretations*; 32-800; Jet Propulsion Laboratory, California Institute of Technology: Pasadena, CA, USA, 1966; pp. 252–263.

38. Neukum, G.; Ivanov, B.A.; Hartmann, W.K. Cratering records in the inner solar system in relation to the lunar reference system. *Space Sci. Rev.* **2001**, *96*, 55–86. [CrossRef]
39. Wu, B.; Wang, Y.; Werner, S.C.; Prieur, N.C.; Xiao, Z. A global analysis of crater depth/diameter ratios on the Moon. *Geophys. Res. Lett.* **2022**, *49*, e2022GL100886. [CrossRef]

Disclaimer/Publisher's Note: The statements, opinions and data contained in all publications are solely those of the individual author(s) and contributor(s) and not of MDPI and/or the editor(s). MDPI and/or the editor(s) disclaim responsibility for any injury to people or property resulting from any ideas, methods, instructions or products referred to in the content.